Res. Lett. **6**, 731 (1979); P. M. Cassen, S. J. Peale, R. T. Reynolds, *ibid.* **7**, 987 (1980); S. W. Squyres, R. T. Reynolds, P. M. Cassen, S. J. Peale, *Nature* **301**, 225 (1983).
6. T. B. McCord *et al.*, *Science* **278**, 271 (1997); T. B. McCord *et al.*, *Eos (Spring Suppl.)* **78**, S202 (abstr.) (1997); T. B. McCord *et al.*, *J. Geophys. Res.* **103**, 8603 (1998).
7. R. T. Reynolds, S. W. Squires, D. S. Colburn, C. P. McKay, *Icarus* **56,** 246 (1983).
8. The main water-ice absorptions were reported at 3.0, 2.0, 1.5, 1.25, and 1.04 μm. For example, G. P. Kuiper, in *The Solar System, 3, Planets and Satellites*, G. P. Kuiper and B. M. Middlehurst, Eds. (Univ. of Chicago Press, Chicago, IL, 1961), pp. 305–306; V. I. Moroz, *Trans. Soviet. Astron. A. J.* **9**, 999 (1965); T. V. Johnson and T. B. McCord, *Astrophys. J.* **169**, 589 (1971); H. H. Kieffer and W. D. Smythe, *Icarus* **21**, 506 (1974); J. B. Pollack *et al.*, *ibid.* **36**, 271 (1978); R. N. Clark, *ibid.* **44**, 388 (1980); *J. Geophys. Res.* **86**, 3087 (1981); *Icarus* **49**, 244 (1982); T. V. Johnson *et al.*, *J. Geophys. Res.* **88**, 5789 (1983). See W. M. Calvin, R. N. Clark, R. H. Brown, and J. R. Spencer [*J. Geophys. Res.* **100**, 19041 (1995)] for the most recently reported data and a review.
9. A. L. Lane, R. M. Nelson, D. L. Matson, *Nature* **292**, 38 (1981); R. M. Nelson *et al.*, *Icarus*, **72**, 358 (1986); R. E. Johnson, M. L. Nelson, T. B. McCord, J. C. Gradie, *ibid.* **75**, 423 (1988); M. K. Pospieszalska and R. E. Johnson, *ibid.* **78**, 1 (1989); N. J. Sack, R. E. Johnson, J. W. Boring, R. A. Baragiola, *ibid.* **100**, 534 (1992).
10. K. F. Noll, A. Weaver, A. M. Gonnella, *J. Geophys. Res.* **100**, 19057 (1995).
11. The Galileo NIMS began spectrometric observations of the Galilean satellites in June 1996. The NIMS covers the wavelength (λ)range 0.7 to 5.2 μm with up to 408 spectral channels and a resolving power of 40 to 200 (λ/Δλ). The instrument's instantaneous field of view is 0.5 mrad, giving a spatial resolution (pixel size) of, for example, 5 km at 10,000-km distance. The spectra are calibrated to units of reflectance at the specific geometry of the observation compared with the reflectance of a perfectly diffusing (Lambert) surface with the use of the solar spectrum and a combination of ground and in-flight NIMS measurements of calibration targets. See R. W. Carlson, P. R. Weissman, W. D. Smythe, J. C. Mahoney, and the NIMS Science and Engineering Team [*Space Sci. Rev*. **60**, 457 (1992)] for a description of the NIMS instrument.
12. R. W. Carlson *et al.*, *Science* **274**, 385 (1996).
13. N. Ockman, *Adv. Phys*. **7**, 199 (1958); W. M. Irvine and J. B. Pollack, *Icarus* **8**, 324 (1968); P. V. Hobbs, *Ice Physics* (Clarendon, Oxford, UK, 1974); S. G. Warren, *Appl. Opt.* **23**, 1206 (1984).
14. For example, G. R. Hunt, J. W. Salisbury, C. J. Lenhoff, *Mod. Geol.* **3**, 1 (1971); *ibid.* **4**, 85 (1973).
15. J. K. Crowley, *J. Geophys. Res.* **96**, 16231 (1991).
16. U. Fink and H. P. Larson, *Icarus* **24**, 411 (1975).
17. R. W. Carlson and the NIMS Team, paper presented at the Workshop on Remote Sensing of Planetary Ices: Earth and Other Solid Bodies, Flagstaff, AZ, 11 to 13 June 1997; R. W. Carlson, paper presented at the Annual Meeting of the Geological Society of America, Salt Lake City, UT, 22 October 1997.
18. This approach ignores many factors affecting the details of reflectance spectra, such as particle size and multiple nonlinear scattering. It is used here to demonstrate some outstanding fundamental properties in a rapid and simple manner.
19. T. B. McCord *et al.*, *Eos (Fall Suppl.)* **78**, F407 (abstr.) (1997); T. B. McCord *et al.*, *Lunar Planet. Sci.* **XXIX**, 1560 (abstr.) (1998). A band-minimum (rather than total band shape) map for one Europa area also was presented by J. C. Granahan *et al.* [*Eos (Fall Suppl.)* **78**, F417 (abstr.) (1997)].
20. For example, J. K. Crowley, *Remote Sensing Environ.* **44**, 337 (1993); *Econ. Geol.* **91**, 622 (1996); R. N. Clark, G. A. Swayze, A. Gallagher, T. V. V. King, W. M. Calvin, *U.S. Geol. Surv. Open File Rep. 93-592* (1993). See these references for descriptions of various minerals.
21. J. C. Granahan *et al.*, *Bull. Am. Astron. Soc*. **29**, 982 (abstr.) (1997); F. P. Fanale *et al.*, in preparation.
22. R. V. Gaines, H. C. W. Skinner, E. E. Foord, B. Mason, A. Rosenzweig, *Dana's New Mineralogy* (Wiley, New York, ed. 8, 1997).
23. W. Hagen, A. G. G. M. Tielens, J. M. Greenberg, *Chem. Phys.* **56**, 367 (1981); W. Hagen and A. G. G. M. Tielens, *Spectrochim. Acta* **38A**, 1089 (1982); W. M. Grundy and B. Schmitt, *J. Geophys. Res.*, in press.
24. For example, L. A. Hardie, *Geochim. Cosmochim. Acta* **32**, 1279 (1968).
25. F. P. Fanale, T. V. Johnson, D. L. Matson, in *Planetary Satellites* (Univ. of Arizona Press, Tucson, AZ, 1977), pp. 379–405; J. S. Kargel, *Icarus* **94**, 368 (1991).
26. F. P. Fanale *et al.*, *Lunar Planet. Sci.* **XXIX**, 1248 (abstr.) (1998).
27. R. Y. Stanier *et al.*, *The Microbial World* (Prentice-Hall, Englewood Cliffs, NJ, 1986), pp. 22–23.
28. For example, see S. Kempe, J. Kazmierczak, E. T. Degens, in *Origin, Evolution and Modern Aspects of Biomineralization in Plants and Animals*, R. E. Crick, Ed. (Plenum, New York, 1989), pp. 29–43.
29. NIMS observations are named for the primary satellite target, the number of the orbit around Jupiter, and the name of the target area on the satellite, for example, E6TERINC = Europa, 6th orbit, Terra Incognito.
30. The water frost albedo model used is from W. J. Wiscombe and S. G. Warren [*J. Atmos. Sci.* **37**, 2712 (1980)], and the optical constants used are described by G. B. Hansen, T. B. McCord, and the NIMS Team [*Lunar Planet. Sci.* **XXVIII**, 505 (abstr.) (1997)].
31. This work was supported in part by the NASA Galileo Project. This is SOEST publication 4622 and HIGP publication 987.

18 February 1998; accepted 13 April 1998

Viscosity of Oceanic Asthenosphere Inferred from Remote Triggering of Earthquakes

Fred F. Pollitz, Roland Bürgmann, Barbara Romanowicz

A sequence of large interplate earthquakes from 1952 to 1965 along the Aleutian arc and Kurile-Kamchatka trench released accumulated stresses along nearly the entire northern portion of the Pacific Plate boundary. The postseismic stress evolution across the northern Pacific and Arctic basins, calculated from a viscoelastic coupling model with an asthenospheric viscosity of 5×10^{17} pascal seconds, is consistent with triggering of oceanic intraplate earthquakes, temporal patterns in seismicity at remote plate boundaries, and space-based geodetic measurements of anomalous velocity over an area 7000 by 7000 kilometers square during the 30-year period after the sequence.

Stress pulses travelling away from an earthquake source area effectively transmit the local stress changes associated with the earthquake to a much larger area as the ductile sublithospheric channel gradually yields with time (*1*–*4*). Several studies have applied such a model to the continental lithosphere, where predictions may be readily compared with geodetic observations [for example, see (*3*–*7*)]. There have also been a few applications suggestive of stress diffusion through the ocean basins (*1*, *2*, *8*). Here we evaluate postseismic stress evolution driven by large subduction events that occurred along the Aleutian and Kurile-Kamchatka trenches from 1952 to 1965 (Fig. 1A) and use the inferred correlation with seismicity to estimate the viscosity of the oceanic asthenosphere. The subduction earthquakes have total seismic moment exceeding 1000×10^{20} N·m and are by far the largest involving the Pacific Plate to have occurred during the period 1950–1970 (*9*). Moreover, each of them occurred on subduction interfaces that had experienced smaller events on time scales of 20 to 90 years but no comparable large ruptures for at least the past 200 years (*10*). Because these events involve only the Pacific–North America plate boundary, stress changes may be evaluated without any significant complications over the entire Pacific basin as well as the Arctic basin (on the North American Plate). We specified the elastic deformation associated with these earthquakes in terms of the fault planes and slip directions shown in Fig. 1A and source parameters from (*11*). We also included a few smaller but significant events with total seismic moment of $\sim 150 \times 10^{20}$ N·m: thrust events along the Kurile/Bonin arc in 1958, 1963, 1968, 1969, 1972, 1973, and 1978, and the 1986 Andreanof Islands earthquake along the Aluetian arc (*12*).

We constructed a rheology appropriate for the oceanic lithosphere from the seismic structure determined by Gaherty *et al.* (*13*) and then calculated postseismic gravitational-viscoelastic relaxation on a grid covering the northern Pacific and Artic basins (*4*). The model implies that for an asthenospheric viscosity of $\eta = 5 \times 10^{17}$ Pa·s, the leading edge of the stress pulse passed by the Juan de Fuca plate in 1975 and California in 1985 (the southward-propagating blue region in Fig. 1). The dispersive character of the propagating stress pulse is such that

F. F. Pollitz and R. Bürgmann, Department of Geology, University of California, Davis, Davis, CA 95616, USA.
B. Romanowicz, University of California Seismological Laboratory, 475 McCone Hall, Berkeley, CA 94720, USA.

regions along the advancing front at a given time experience locally high horizontal velocities (*3*, *4*). Thus, the fronts of spatially maximal strain rate and temporally maximal velocity nearly coincide. Although the former is most useful for demonstrating the pulselike behavior of the stress diffusion process, the latter provides a physical connection between stress diffusion within the oceanic plate and induced strains at or across adjacent plate boundaries.

Passage of the predicted velocity front is correlated with spatiotemporal patterns in seismicity in western North America over the past four decades, provided that asthenospheric viscosity is close to 5×10^{17} Pa·s. Seismic activity may be adequately represented as simply a function of time and latitude. From a suitable catalogue (*14*) spanning the time period 1963–1996 at magnitudes above body wave magnitude (M_b) = 5.3, let t_{eq} (i) and lat_{eq} (i) be the time of occurrence and latitude, respectively, of the ith earthquake. Similarly, we define lat_{vel} (t) as the latitude of areas just adjacent to the Pacific margin off western North America that experience a velocity maximum at time t. In order to test how consistent this catalogue is with the southward progression of the velocity front, we construct the correlation function in latitude-time space

$$f(\mathrm{lat},t) = \frac{1}{A(\mathrm{lat},t)} \sum_i M_b(i) \qquad (1)$$

where the summation is for events i that satisfy

$$\mathrm{lat}_{vel}(t_{eq}(i)) + \mathrm{lat} - \mathrm{lat}_{vel}(t) - 3.0° < \mathrm{lat}_{eq}(i) < \mathrm{lat}_{vel}(t_{eq}(i)) + \mathrm{lat} - \mathrm{lat}_{vel}(t) + 3.0° \qquad (2)$$

The inequality condition in Eq. 2 effectively sweeps out a latitude band 6° in width that is parallel to the lat_{vel} (t) versus t curve and sums the magnitude of earthquakes occurring within that band. The normalization factor A(lat,t) is proportional to the area swept out by this band and corrects for the fact that bands near the corners of the latitude-time window are smaller than those near the middle diagonal. This correlation function enforces a strictly banded structure parallel to lat_{vel} (t). An alternative definition of Eq. 1 could involve either number of events or seismic moment rather than M_b, but results are similar in all cases. As shown in Fig. 2, the observed seismicity is correlated with passage of the velocity front generated by the great Aleutian and Kurile-Kamchatka events of 1952 to 1965. The structure of f (lat,t) is asymmetric about its maximum central band, implying, if our

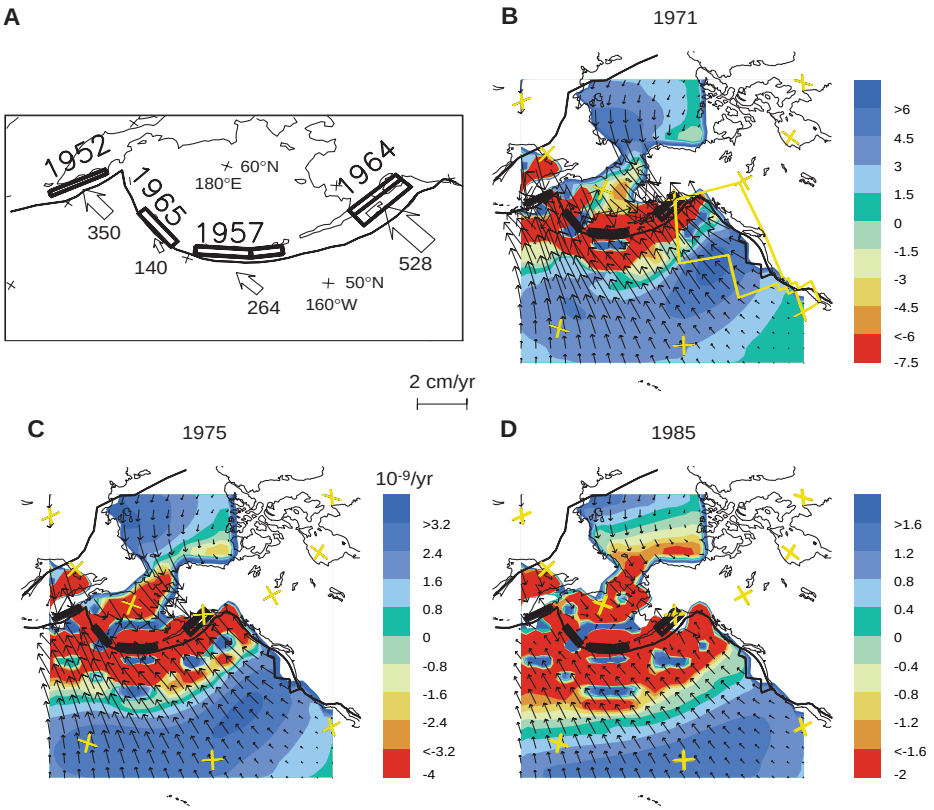

Fig. 1. (**A**) Rupture areas of major subduction events along the Aleutian arc and Kamchatka trench from 1952 to 1965. Arrows give the direction of slip associated with each of the four events considered, with length proportional to total seismic moment. Numerals adjacent to these arrows specify the seismic moment in units of 10^{20} N·m (*30*). (**B** through **D**) Net postseismic velocity and dilatational strain rate $\dot{e}_{EE}+\dot{e}_{NN}$ (E, east; N, north) over the northern Pacific and eastern Arctic basins driven by combined subduction events projected onto a sphere centered on 50°N, 155°W as evaluated at three different times. Deformation is evaluated at Earth's surface. Heavy lines denote the fault planes used to model the subduction events. Locally large velocities near the rupture zones have been truncated at a maximum of 5 cm year^{-1} for visual simplicity.

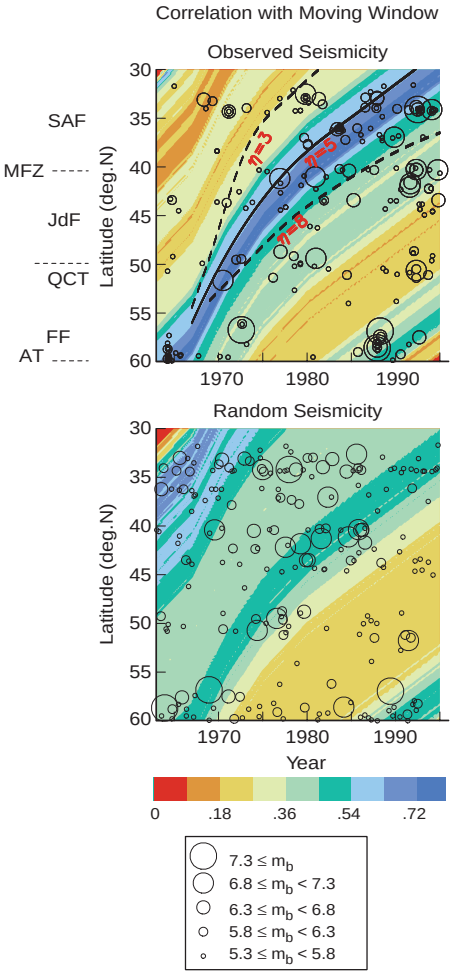

Fig. 2. Observed western North America seismicity from 1963 to 1995 is represented in terms of location (latitude), time t, and M_b as given by the size of the circles. Correlation function f (lat,t) (Eq. 1) was obtained with either an observed or a random seismicity catalogue. In the latter case, the structure of the observed seismicity is altered such that lat_{eq} (i) is unchanged while t_{eq} (i) becomes a random function of time obeying the uniform distribution between the years 1963 and 1995. The shape of the velocity front lat_{vel} (t) for η = 3, 5, or 8 × 10^{17} Pa·s is indicated. Almost all seismic events used (restricted to the boxed region of Fig. 1B) are associated with the active eastern Pacific margin. AT, Aleutian Trench; FF, Fairweather Fault; JdF, Juan de Fuca Plate; MFZ, Mendocino Fracture Zone; QCT, Queen Charlotte Transform Fault; SAF, San Andreas Fault.

model is correct, that passage of the front generally initiated vigorous seismic activity in a given region, and seismic activity continued for a number of years. This analysis cannot discriminate between continued activity triggered directly by the velocity front and secondary activity triggered by stress changes generated by the initial activity, but it does suggest that accumulated transient displacement (time-integrated transient velocity) along a particular plate margin plays an important role.

Ultimately, of course, it is accumulated stress changes that probably trigger earthquakes. At a neighboring mid-ocean ridge system such as the Juan de Fuca ridge system, lithospheric thickness shallows to less than 5 km, and partially molten material distributed in magma chambers and dikes is present. It seems likely that an increase in velocity of one of the bounding oceanic plates would lead to rapid stress concentration in the axial rift zone and subsequent seismic or aseismic failure of the rift segments at anomalously high rates. Increased seismicity rates on short offset transform faults such as the Blanco and Mendocino fracture zones may similarly result from intense stress concentration in the weak transform fault zone, compounded by loading from the more rapidly opening rift zones that bound them. Finally, near an ocean-continent boundary such as just west of the San Andreas Fault (SAF), the upper crust is likely to be weaker than the oceanic lithosphere with which it is in contact, and the lower crust is also weak. In this case, strains induced on the continental side should depend predominantly on the local displacement of the oceanic side, although the mechanism of strain accumulation within the continental crust is uncertain.

Predicted postseismic North American plate velocity has generally been directed away from both the eastern Arctic and Juan de Fuca spreading systems, promoting rifting, and reached peaks in the late 1970s in both regions. If the background North America–to–Eurasia separation rate is prescribed by the model NUVEL-1A (*15*) and postseismic velocity is presumed to represent transient North American velocity with respect to a fixed Eurasia, then the background and transient velocities may be superimposed to obtain a time-dependent separation rate. The transient component is predicted to have been up to 1 cm year^{-1} in the eastern Arctic basin, where the background component varies from 0.4 to 1.2 cm year^{-1}. Seismicity patterns of all eastern Arctic events with $M_b \geq 5.0$ [since 1955, from which date the catalogue is believed to be complete for $M_b \geq 5.0$ (*16*)] exhibit a good correlation with the summed velocity pattern (Fig. 3A). Seismicity rates along the entire eastern Arctic ridge system exhibit an increase from one time period to the next, and the part of the oceanic rift system nearest the Asian continent underwent the largest velocity increase and largest increase in seismicity rate, as measured by moment release.

In central California (35° to 39°N), the transient Pacific plate motion is predicted to have reached a maximum 2.6 mm year^{-1}, toward N40°W in 1980–1985 (parallel to the SAF); and in southern California south of the Big Bend region (32° to 35°N), the transient motion is predicted to have reached a maximum of 1.7 mm year^{-1} toward N39°W in 1985–1990 (25° to 30° oblique to the SAF, increasing compressional stress across the fault system near the Big Bend) (Fig. 3B). The direction of transient motion in both regions is nearly parallel to the background motion prescribed by NUVEL-1A. In northern California, the transient velocity increase, as manifested by the accumulated transient displacement, is well correlated with the observed increase in predominantly strike-slip activity. In southern California, the temporal increase in observed seismicity since the 1971 San Fernando earthquake also closely follows accumulated displacement. Although the overall seismicity rate in southern California was approximately constant from 1969 to 1992 (*17*), between latitudes 34°N and 35°N the rate of occurrence of non-SAF–

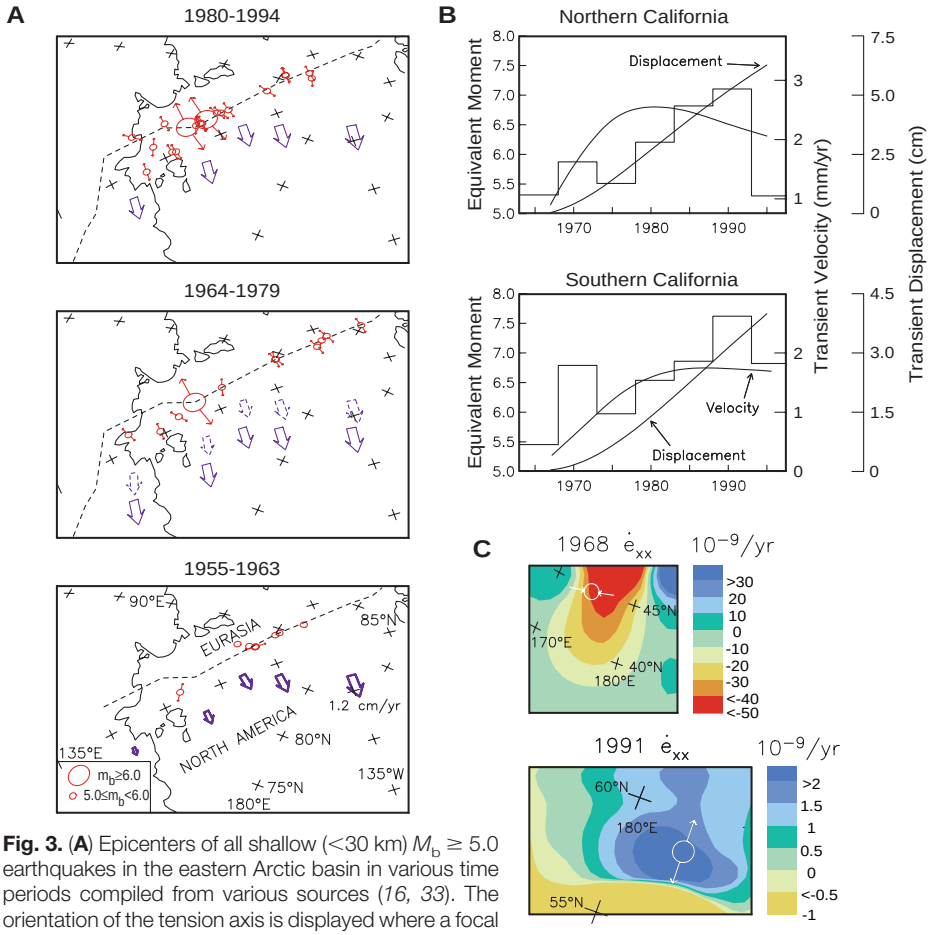

Fig. 3. (**A**) Epicenters of all shallow (<30 km) $M_b \geq 5.0$ earthquakes in the eastern Arctic basin in various time periods compiled from various sources (*16, 33*). The orientation of the tension axis is displayed where a focal mechanism solution is available. Heavy arrows plotted for 1955–1963 indicate background motion of the North America plate to the fixed Eurasia plate (*15*); dashed and solid arrows for 1964–1979 indicate the background plus transient (postseismic) relative plate motion evaluated in 1967 and 1975, respectively; and the solid arrows for 1980–1994 indicate the background motion plus transient relative plate motion evaluated in 1985. The East Arctic ridge separating the North American and Eurasian plates is indicated by the dashed lines. (**B**) Equivalent magnitude *M* of summed seismic moment M_0 within binned 5-year intervals in northern California (latitudes 35° to 39°N) and southern California (32° to 35°N), derived from all regional earthquakes within the boxed region of Fig. 1B of magnitude ≥ 5.0 (*14*) and the averaged seismic moment formula of (*34*). Time-dependent transient velocity and displacement of the adjacent Pacific margin lithosphere are superimposed. (**C**) Geographic distribution of net postseismic strain rate $\dot{e}_{xx}$ in the vicinity of the M_b = 5.5 (28 April 1968) and the M_b = 6.8 (21 February 1991) Bering Sea earthquakes, where *x* is oriented parallel to either the pressure axis with azimuth N77°E (the 1968 event) or the tension axis with azimuth S2°W (the 1991 event).

type events has been particularly high since 1986 (*18*). This increase in non-SAF–type events has been attributed (*18*) to a transient increase in the component of Pacific–to–North America (P-NA) relative plate velocity that is normal to the SAF in southern California, and our model provides a mechanism for this transient increase.

Although there may be a correlation of plate-boundary seismicity over the entire western North America margin with the predicted stress pulse propagation in the adjacent Pacific oceanic lithosphere, it does not imply a causal mechanism for every earthquake but rather a causal relationship with transient oceanic velocity in a statistical sense. Our analysis therefore suggests, but does not require, a major role for external triggering of California earthquakes since about 1979. This idea connects well with the hypothesis that northern California emerged from the stress shadow created by the 1906 San Francisco earthquake in the 1980s (*19*), making the region particularly susceptible to external triggering. The triggering of California earthquakes at a relatively high threshold ($M_b \geq 5.0$ to 5.3), as implied by our analysis, suggests that a transient velocity increase applied to the edge of a continental shear zone may concentrate transient stresses deep within the seismogenic layer (15 to 20 km depth) where larger events are typically initiated. Efforts to identify the predicted accelerations (about 2 mm year^{-1} over the period 1965/1970–1980/1985) are inconclusive. Accurate space-based geodetic data have been available since 1983 in California, at which time most of the acceleration had already taken place. Repeated geodolite measurements made since the early 1970s within several southern California networks (*20*) may have potential for resolving a transient acceleration, but the small signal that we predict is likely to be at the limit of detectability of these networks.

Two intraplate oceanic earthquakes may have been triggered by the postseismic stress diffusion. These are the $M_b = 5.5$ event on 28 April 1968 in the northern Pacific basin, which has a thrust mechanism (*21*), and the $M_b = 6.8$ Bering Sea earthquake on 21 February 1991, characterized as a combined strike-slip and rifting event (*22*). By calculating the geographic distribution of strain rate $\dot{e}_{xx}$, where x is oriented parallel to either the pressure axis (the 1968 event) or tension axis (the 1991 event), we find that each event is located in a region where local strain rates promoting triggering were strong at their time of occurrence (Fig. 3C). The associated accumulated postseismic stress change σ_{xx} is calculated at 0.3 and 0.8 bars for the 1968 and 1991 events, respectively. Such a stress change is often sufficient to trigger comparable continental seismicity (*23*), especially considering that the respective source areas were probably preexisting zones of weakness (*22, 24*).

The correlations with the oceanic intraplate events in Fig. 3C are found to break down for $\eta < 3 \times 10^{17}$ Pa•s, whereas $\eta > 8 \times 10^{17}$ Pa•s still produces correlations but involves stress changes one order of magnitude lower. The obtained correlations with western North American seismicity imply that if $\eta = 8 \times 10^{17}$ Pa•s, then most of the acceleration in seismic activity would take place long before passage of the velocity front, and if $\eta = 3 \times 10^{17}$ Pa•s, most seismic activity would occur long after it; the notion that transient rates are relatively high for $\eta = 3 \times 10^{17}$ Pa•s would further aggravate this problem. A similar argument applies to east Arctic ridge seismicity. Finally, to produce the same diffusion behavior with a thicker lithosphere would require greater asthenospheric viscosity. Given our choice for the lithospheric thickness, our preferred value is $\eta = 5 \times 10^{17}$ Pa•s, which is compatible with the data in the Arctic and north Pacific basins. The overall viscosity structure we infer (*13*) agrees well with the viscosity structure beneath a mid-ocean ridge, based on the physical properties of wet olivine aggregates (*25*). Our results imply that the evolution of off-ridge-axis oceanic mantle preserves the essential features of the ridge-axis viscosity structure. Small-scale convection, which may act to "flatten" age-depth and age-heat flow relationships for the oceanic lithosphere (*26*), may produce a similar flattening of the off-ridge viscosity structure.

Detectable transient velocities are predicted even very far (~4000 km) from the Aleutian trench in the mid-Pacific, where Global Positioning System (GPS) and Very Long Baseline Interferometry (VLBI) data can be evaluated. Figure 4A shows P-NA anomalous horizontal velocity at several Pacific geodetic sites, with relative motion model NUVEL-1A serving as the reference model (*27*). The predictions of the viscoelastic coupling model are superimposed. The general agreement between the internal Pacific strain patterns prescribed by our model and the geodetic observations is best demonstrated by referring the anomalous velocities obtained in Fig. 4A to a different P-NA angular velocity vector ω which we derive (*28*). The anomalous velocities relative to the derived ω are shown in Fig. 4B. An objective measure of the internal deformation of the Pacific plate based on these geodetic measurements is

$$\sigma^2 = \frac{1}{12} \sum_{i=1}^{12} (\gamma_i)^2 + (\beta_i)^2 \qquad (3)$$

where $\{\gamma_i\}$ and $\{\beta_i\}$ represent the set of all

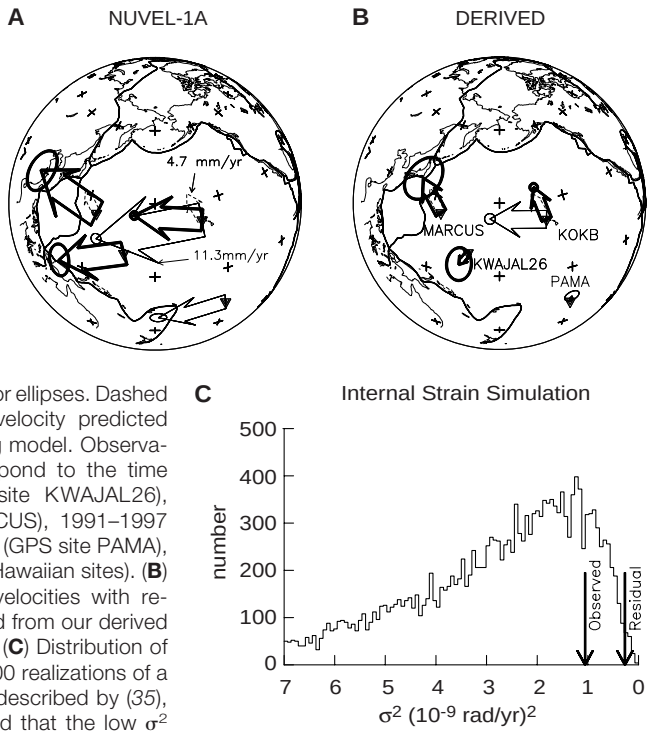

Fig. 4. (**A**) Anomalous GPS (light arrows) and VLBI (heavy arrows) velocities with respect to the P-NA velocity predicted from model NUVEL-1A. VLBI velocity plotted at KOKB has been averaged over three Hawaiian VLBI sites. These anomalous velocities have been derived from GPS and VLBI velocities at Pacific and selected North American sites. Observed anomalous velocities are shown with the corresponding 1σ error ellipses. Dashed arrows show the transient velocity predicted from our viscoelastic coupling model. Observations and predictions correspond to the time periods 1984–1988 (VLBI site KWAJAL26), 1988–1992 (VLBI site MARCUS), 1991–1997 (GPS site KOKB), 1992–1997 (GPS site PAMA), and 1984/1993–1996 (VLBI Hawaiian sites). (**B**) Anomalous GPS and VLBI velocities with respect to the velocity predicted from our derived P-NA angular velocity vector. (**C**) Distribution of σ^2 (Eq. 3) resulting from 10,000 realizations of a data perturbation procedure described by (*35*), designed to test the likelihood that the low σ^2 obtained after accounting for our calculated transient effects could be due to chance.

angle changes and relative arc length changes among all four spherical triangles that can be constructed from the four mid-Pacific geodetic sites. This measure is invariant with respect to a rigid rotation of the velocity field and contains information on mean shear strain and dilatation within this broad network. The mean observed σ^2 is 1.06 $(10^{-9}$ rad$)^2$, and after correction for transient velocities this measure decreases to 0.27 $(10^{-9}$ rad$)^2$; that is, a reduction of 75%. A numerical perturbation simulation using the error distribution of the data shows that the probability that this reduction could be explained with observation error alone is 0.7% (Fig. 4C).

Although geodetic observations made near plate boundaries are often acknowledged as being susceptible to the transient effects of earthquakes, our analysis suggests that even areas well within a plate interior may be susceptible to substantial and tangible transient effects from plate boundary earthquakes. Our model makes concrete predictions regarding transient Pacific Plate velocity that are testable with present and future space-based geodetic data. From the results obtained here, it appears likely that the Pacific lithosphere has been subjected to substantial spatially and temporally varying velocity fluctuations over the past four decades, and that the assumption of rigid behavior of the oceanic lithosphere, which has been so successful in explaining global plate motions averaged over very long time periods, may be of questionable validity on a time scale of years to decades.

REFERENCES AND NOTES

1. W. M. Elsasser, in *The Application of Modern Physics to the Earth and Planetary Interiors*, S. K. Runcorn, Ed. (Wiley, New York, 1969), pp. 223–246.
2. D. L. Anderson, *Science* **187**, 1077 (1975).
3. P. A. Rydelek and I. S. Sacks, *Geophys. J. Inter.* **100**, 39 (1990); S. C. Cohen, *J. Geophys. Res.* **97**, 15395 (1992).
4. F. F. Pollitz, *J. Geophys. Res.* **102**, 17921 (1997).
5. P. A. Rydelek and I. S. Sacks, *Nature* **336**, 234 (1988).
6. C. O. Sanders, *Science* **260**, 973 (1993).
7. W. Thatcher, T. Matsuda, T. Kato, J. B. Rundle, *J. Geophys. Res.* **85**, 6429 (1980); K. Miyashita, *J. Phys. Earth* **35**, 449 (1987); T. Tabei, *ibid.* **37**, 101 (1989); F. F. Pollitz and I. S. Sacks, *ibid.* **42**, 1 (1994); A. Piersanti, G. Spada, R. Sabadini, *J. Geophys. Res.* **102**, 477 (1997).
8. J. C. Savage, *J. Geophys. Res.* **76**, 1954 (1971); H. J. Melosh, *ibid.* **81**, 5621 (1976); E. Berg, G. H. Sutton, D. A. Walker, *Tectonophysics* **39**, 559 (1977); B. Romanowicz, *Science* **260**, 1923 (1993).
9. Although the 1960 Chilean earthquake is larger than all of these events combined, the presence of the East Pacific Rise as the Pacific–Nazca Plate boundary is likely to decouple its effects from the surrounding Pacific basin.
10. S. P. Nishenko and K. H. Jacob, *J. Geophys. Res.* **95**, 2511 (1990); C. G. Bufe, S. P. Nishenko, D. J. Varnes, *Pure Appl. Geophys.* **142**, 83 (1994).
11. F. T. Wu and H. Kanamori, *J. Geophys. Res.* **78**, 6082 (1973); H. Kanamori, *Phys. Earth Planet. Int.* **11**, 216 (1976); S. L. Beck and D. H. Christensen, *J. Geophys. Res.* **96**, 2205 (1991); D. H. Christensen and S. L. Beck, *Pure Appl. Geophys.* **142**, 29 (1994); S. R. Holdahl and J. Sauber, *ibid.* **142**, 54 (1994). Both the 1957 and 1964 rupture zones are divided into two fault planes in order to more accurately represent their overall ruptures. The assignment of uniform moment tensor density on each fault plane is adequate for the intended application.
12. H. Kanamori, *J. Geophys. Res.* **75**, 5011 (1970); *Tectonophysics* **12**, 1 (1971); K. Abe, *Phys. Earth Planet. Inter.* **7**, 143 (1973); K. Shimazaki, *ibid.* **9**, 314 (1974); Y. Fukao and M. Furumoto, *Geophys. J. R. Astron. Soc.* **57**, 23 (1979); T. Seno *et al*., *Phys. Earth Planet. Inter.* **23**, 39 (1980); D. Giardini, A. Dziewonski, J. Woodhouse, *ibid.* **40**, 259 (1985); T. M. Boyd and J. L. Nabelek, *Bull. Seismol. Soc. Am.* **78**, 1653 (1988). A seismic moment of 10×10^{20} N m^{-1} was assigned to the 1986 Andreanof Islands earthquake.
13. J. B. Gaherty, T. H. Jordan, L. S. Gee, *J. Geophys. Res.* **101**, 22291 (1996). The rheological structure of the oceanic lithosphere and underlying mantle is prescribed as follows: Layer 1 (0 to 8 km depth): $\lambda = \mu = 35$ GPa, $\rho = 2900$ kg m^{-3} (purely elastic). Layer 2 (8 to 62 km depth): $\lambda = \mu = 65$ GPa, $\rho = 3400$ kg m^{-3} (purely elastic). Layer 3 (62 to 213 km depth): Lame parameters $\lambda = \mu = 75$ GPa, density $\rho = 3400$ kg m^{-3}, viscosity $= \eta$ (viscoelastic asthenosphere). Layer 4 (below 213 km depth): $\lambda = \mu = 75$ GPa, $\rho = 3400$ kg m^{-3}, viscosity $= 1000 \times \eta$. A Maxwell rheology is taken for the asthenosphere, conforming to deformation of olivine in the diffusion creep regime (*29*). The total thickness of the elastic oceanic lithosphere of 62 km is only slightly smaller than the 68-km estimate of the depth to the mid-Pacific low-velocity zone defined by a sharp boundary, and it is about twice as large as the effective elastic plate thickness of the oceanic lithosphere based on observations of flexure [A. B. Watts, J. H. Bodine, N. M. Ribe, *Nature* **283**, 532 (1980); M. K. McNutt and H. W. Menard, *Geophys. J. R. Astron. Soc.* **71**, 363 (1982)]. Although the base of the asthenosphere is not well defined seismically, a large viscosity increase probably occurs at a depth of 200 to 250 km because of the pressure dependence of the viscosity of olivine (*29*).
14. U.S. Geological Survey, National Earthquake Information Center Catalogue (USGS, Menlo Park, CA, 1998).
15. C. DeMets, R. Gordon, D. Argus, S. Stein, *Geophys. Res. Lett.* **21**, 2191 (1994).
16. J. H. Hodgeson *et al*., *Ann. Int. Geophys. Year* **30**, 33 (1965); K. Fujita, D. B. Cook, H. Hasegawa, D. Forsyth, R. Wetmiller, in *The Decade of North American Geology, Vol. L*, L. Grantz, L. Johnson, J. F. Sweeney, Eds. (Geological Society of America, Boulder, CO, 1990), pp. 79–100.
17. L. K. Hutton and L. M. Jones, *Bull. Seismol. Soc. Am.* **83**, 313 (1993); L. M. Jones and E. Hauksson, *Geophys. Res. Lett.* **24**, 469 (1997).
18. F. Press and C. Allen, *J. Geophys. Res.* **100**, 6421 (1995).
19. S. C. Jaume and L. R. Sykes, *ibid.* **101**, 765 (1996). The Queen Charlotte and Fairweather faults, by contrast, were subjected to ~10 times higher transient velocity of the adjacent oceanic lithosphere than was California, but they exhibited far less triggered seismicity (Fig. 2). Large earthquakes on these faults (*M* 8.1 in 1949 and *M* 7.9 in 1958) created a stress shadow that has enveloped the fault system ever since, except for a gap that was filled by the 1972 Sitka earthquake [M. M. Schell and L. J. Ruff, *Phys. Earth Planet. Int.* **54**, 241 (1989)].
20. J. C. Savage, *J. Geophys. Res.* **100**, 12691 (1995).
21. L. R. Sykes and M. L. Sbar, in *Geodynamics of Iceland and the North Atlantic*, L. Kristjansson, Ed. (Reidel, Dordrecht, Netherlands, 1974), pp. 207–224.
22. G. A. Abers, G. Ekstrom, M. S. Marlow, E. L. Geist, *J. Geophys. Res.* **98**, 2155 (1993). Most of the cumulative stress change evaluated in the Bering Sea arises from the 1957 event in our model (the contribution of the 1957 event to σ_{xx} is 0.77 bars; the contribution of the 1986 event is 0.04 bars), but nearly all of the strain rate predicted in 1991 arises from the 1986 Andreanof Islands earthquake.
23. G. C. King, R. S. Stein, J. Lin, *Bull. Seismol. Soc. Am.* **84**, 935 (1994).
24. E. A. Bergman and S. C. Solomon, *J. Geophys. Res.* **85**, 5389 (1980).
25. G. Hirth and D. L. Kohlstedt, *Earth Planet. Sci. Lett.* **144**, 93 (1996). Our preferred viscosity value also lies within the range 4×10^{17} to 3×10^{18} Pa·s, determined from thermal constraints on small-scale convection [A. Davaille and C. Jaupart, *J. Geophys. Res.* **99**, 19853 (1994)].
26. B. Parsons and J. G. Sclater, *J. Geophys. Res.* **82**, 803 (1977); C. A. Stein and S. Stein, *Nature* **359**, 123 (1992).
27. The geodetic data consists of GPS data [K. Larson, personal communication] at KOKB on Hawaii and PAMA on Pamatai, plus VLBI data [publicly available at http://lupus.gsfc.nasa.gov/vlbi.html] at KWAJAL26, MARCUS, and three Hawaiian sites. The three VLBI observations at Hawaiian sites have been averaged into a single observation. We define stable North America for the GPS data set by minimizing velocity at the seven North American GPS sites considered stable by Larson *et al*. [K. Larson, J. T. Freymuller, S. Philipsen, *J. Geophys. Res.* **102**, 9961 (1997)]. A similar procedure is applied separately to the VLBI data set.
28. We perform an inversion for the best-fitting P-NA angular velocity vector ω using transform azimuth data from the Gulf of California [C. DeMets, R. G. Gordon, D. F. Argus, S. Stein, *Geophys. J. Int.* **101**, 425 (1990)], the recently revised Gulf of California spreading rate of 5.1 cm year^{-1} [C. DeMets, *Geophys. Res. Lett.* **22**, 3545 (1995)], and the geodetic observations shown in Fig. 4A. The newly derived ω (52.1°S, 100.0°E, 0.79° per million years) predicts Gulf of California spreading rates of 5.1 cm year^{-1} and fits the Gulf of California transform azimuths equally as well as model NUVEL-1A.
29. J.-I. Karato, D. C. Rubie, H. Yan, *J. Geophys. Res.* **98**, 9761 (1993).
30. The fault parameters of the various fault planes representing these events are as follows: 4 November 1952: $\delta = 30°$, $h_2 = 40$ km, $h_1 = 5$ km; 9 March 1957: (eastern+western planes) $\delta = 18°$, $h_2 = 35$ km, $h_1 = 5$ km; 28 March 1964: (shallow plane) $\delta = 5.7°$, $h_2 = 20$ km, $h_1 = 5$ km, (deeper plane) $\delta = 11.3°$, $h_2 = 35$ km, $h_1 = 20$ km; 24 January 1965: $\delta = 18°$, $h_2 = 35$ km, $h_1 = 5$ km where δ is dip and h_2 and h_1 are the depths of the lower and upper fault edges, respectively. The two planes chosen for the 1957 event fill in an 880-km-long section of the Aleutian arc corresponding to the total aftershock area compiled by (*30*) but excluding the easternmost aftershock activity. In choosing this fault length, which involves extending coseismic rupture considerably eastward of the limit of main shock deformation (*31*), we suppose that the total static offset associated with such a large event is defined by the main shock plus the significant aftershocks, which may involve a considerable amount of aseismic slip. Given the large aftershock area, we scale M_0 for the 1957 earthquake up relative to that determined by (*31*) in order to reflect the greater effective fault length.
31. T. M. Boyd, E. R. Engdahl, W. Spence, *J. Geophys. Res.* **100**, 621 (1995).
32. J. M. Johnson *et al*., *Pure Appl. Geophys.* **142**, 3 (1994).
33. L. R. Sykes, *Bull. Seism. Soc. Am.* **55**, 501 (1965); L. A. Savostin and A. M. Karasik, *Tectonophysics* **74**, 111 (1981); J. P. Jemsek, E. A. Bergman, J. L. Nabelek, S. C. Solomon, *J. Geophys. Res.* **91**, 13993 (1986); Harvard Centroid Moment Tensor Catalogue (Harvard University, Cambridge, MA, 1997).
34. T. C. Hanks and H. Kanamori, *J. Geophys. Res.* **84**, 2348 (1979).
35. F. F. Pollitz and I. S. Sacks, *ibid.* **101**, 17771 (1996).

36. This work was supported by the Cooperative UC/Los Alamos Research program and a Presidential Young Investigators award to L. Kellogg. We thank K. Larson for recomputing GPS velocities, D. Argus and J. Melosh for discussions, J. Savage for a critical review, and S. Sacks and P. Rydelek for helpful comments. This research made use of NASA Goddard Space Flight Center's VLBI terrestrial reference frame solution number 1033a3.

21 January 1998; accepted 25 March 1998